

An arbitrary boundary with ghost particles incorporated in coupled FEM–SPH model for FSI problems



Ting Long^{a,b}, Dean Hu^{a,b,*}, Detao Wan^{a,b}, Chen Zhuang^{a,b}, Gang Yang^{a,b}

^a State Key Laboratory of Advanced Design and Manufacturing for Vehicle Body, Hunan University, Changsha 410082, PR China

^b Key Laboratory of Advanced Design and Simulation Technology for Special Equipments, Ministry of Education, Hunan University, Changsha, 410082, PR China

ARTICLE INFO

Article history:

Received 2 November 2016

Received in revised form 23 July 2017

Accepted 22 August 2017

Available online 30 August 2017

Keywords:

Ghost particle method

Coupled FEM–SPH model

Arbitrary boundary

First-order consistency

FSI problems

ABSTRACT

It is important to treat the arbitrary boundary of Fluid–Structure Interaction (FSI) problems in computational mechanics. In order to ensure complete support condition and restore the first-order consistency near the boundary of Smoothed Particle Hydrodynamics (SPH) method for coupling Finite Element Method (FEM) with SPH model, a new ghost particle method is proposed by dividing the interceptive area of kernel support domain into subareas corresponding to boundary segments of structure. The ghost particles are produced automatically for every fluid particle at each time step, and the properties of ghost particles, such as density, mass and velocity, are defined by using the subareas to satisfy the boundary condition. In the coupled FEM–SPH model, the normal and shear forces from a boundary segment of structure to a fluid particle are calculated through the corresponding ghost particles, and its opposite forces are exerted on the corresponding boundary segment, then the momentum of the present method is conservation and there is no matching requirements between the size of elements and the size of particles. The performance of the present method is discussed and validated by several FSI problems with complex geometry boundary and moving boundary.

© 2017 Elsevier Inc. All rights reserved.

1. Introduction

Fluid–structure interaction (FSI) is an important field in the applied science of aerospace, ocean engineering, biomechanics and etc. [1–3]. In general, the interface geometries of practical FSI problems are complex and require robust numerical technique to obtain reasonable solutions [4]. In the past several decades, many numerical methods have been proposed for the FSI problems based on Eulerian framework, such as the Finite Difference Method (FDM) [5], Finite Volume Method (FVM) [6] and Arbitrary Lagrangian Eulerian (ALE) method [7,8]. All of these Eulerian-based methods require considerable time consuming to track the moving boundary or interface [7–9]. Purely Lagrangian methods can naturally handle the moving boundary for FSI problems, but there exist element distortion for traditional Finite Element Method (FEM) in solving large deformation problems, especially for the extreme motion of fluid. In recent years, the FEM has been coupled with Smoothed Particle Hydrodynamics (SPH) to investigate the FSI problems [10–13], which integrate the advantages of success application of FEM for solving structural dynamics and convenience of SPH for simulating fluid dynamics.

* Corresponding author at: State Key Laboratory of Advanced Design and Manufacturing for Vehicle Body, Hunan University, Changsha 410082, PR China.
E-mail address: hudean@hnu.edu.cn (D. Hu).

The SPH method is a purely Lagrangian meshless technique, which has been originally developed in 1977 by Lucy [14], Monaghan and Gingold [15,16]. It has been successfully employed in a wide range of engineering problems in the fields of astrophysics, fluid mechanics, impact dynamics and etc. As the intrinsic nature of kernel-based interpolation and Lagrangian approach, treating boundary condition is one of the great challenging parts of the SPH method. Many methods for implementing boundary condition have been developed, these methods fall into three broad categories:

(1) Repulsive Walls. A repulsive force is exerted on fluid particles, which aims to push all fluid particles away from the walls when they approach to solid wall boundary [17–19].

(2) Ghost Particles. Ghost particles are placed outside the simulation domain, and its prescribed physical quantities (such as pressure and velocity) act to enforce no-slip or free-slip condition [20–23].

(3) Kernel Correction. The missing area of the kernel support domain and boundary integral terms is considered explicitly in the SPH equations [24–26].

All of these methods have advantages and drawbacks. The repulsive walls are easy to implement, even for complex geometries, and are computationally cheap. However, as they only apply repulsive forces away from the boundary, they cannot reproduce systems under tension and capture shear stress felt by fluids on the boundary. Kernel correction type boundaries, such as semi-analytical boundaries based on a variational formulation, was introduced by Kulasegaram et al. [24]. This method was further developed by Ferrand and Mayrhofer et al. [25,27]. Kernel correction has the advantage of restoring zero consistency in the SPH interpolation. However, Mayrhofer et al. [27] showed that semi-analytical boundary conditions only approximately satisfy the skew-adjoint property which is a necessary criterion for energy conservation. Ghost particle method is capable of handling tension, shear stresses and surfaces forces. Recently, Barker et al. [23] proposed a reflected ghost particle boundary accounting for the ‘volume-factor’ for B-splines and curved geometries. Fourtakas et al. [22] proposed an extended modified virtual boundary particle method (eMVBP) based on modified virtual boundary particle method (MVBP) to approximate zeroth-order and first-order consistency in the presence of 2-D irregular boundaries. However, there is no a ghost particle method for complex geometry boundary of structure discretized by elements in coupled FEM with SPH (FEM–SPH) model.

The FEM–SPH model was first proposed by Attaway et al. [28] to study on structure–structure impact problems, they used an iterative master-slave scheme to treat contact force. Vuyst et al. [10] used FEM–SPH model to investigate fluid–structure impact problems by using contact potential to treat contact force. The FEM–SPH model has also been applied to free-surface flow interaction with elastic structures by Groenenboom and Cartwright [11], Fourrey [12] and Jones et al. [13]. Groenenboom and Cartwright [11] used a non-iterative master-slave scheme to treat contact force. Jones et al. [13] used Monahan boundary condition to treat contact force. Fourrey et al. [12] used the ghost particles scheme to compute the pressure from the fluid side. In their methods, the ghost particle scheme has some advantages compared with other methods, it can easily implement no-slip boundary condition and can provide normal and shear forces for fluid unlike other methods only providing normal contact force. So, coupling FEM with SPH using the ghost particle scheme is a very attractive method. However, for no-slip boundary condition, Fourrey et al. [12] calculated the pressure from the fluid side and then exerted the pressure on the structure, there is no shear stress exerted on the structure. But the force from structure to fluid through ghost particles provided the tangential force. Then the forces from the structure to fluid are not equal to the forces from fluid to structure, the equation of momentum is not conservation. Moreover, even for slip boundary condition, there are also exhibited that the forces from structure to fluid are not equal to the forces from fluid to structure, the conservation of momentum equation is not strictly satisfied. There are already several coupled FEM–SPH methods which use ghost particles and are able to achieve conservation for impact dynamics simulation [29–31], these methods can also be used for FSI simulations. For these ghost particle methods, Fourtakas et al. [22] pointed out that the kernel of the boundary particles might not be complete and can produce a very inaccurate SPH interpolation. Moreover, the size of elements should match the size of the particles in these ghost particle methods and they are difficult to handle complex geometry boundary.

In this paper, a ghost particle method is proposed for coupled FEM–SPH model to treat the complex geometry boundary and moving boundary discretized by elements. In the coupled FEM–SPH model, the interceptive area of kernel support domain is divided into subareas based on the corresponding boundary segments. The subareas are used to produce the corresponding ghost particles. Then, the interaction between boundary segments of FEM elements and particles of SPH is evaluated through the corresponding ghost particles. In order to satisfy the conservation of momentum equation, the normal and shear forces from the structure to the fluid are equal to the forces from the fluid to the structure, which is different compared with the ghost particle scheme proposed by Fourrey et al. [12].

This paper is organized as follows. Firstly, the structure theory of the FEM applied to large deformation cases is briefly presented. Secondly, the SPH formulations for the fluid domain are described. Thirdly, the issues of particle inconsistency near the boundary are addressed. Fourthly, the new ghost particle method and the method for coupled FEM–SPH model are presented, respectively. Finally, the numerical results are discussed followed by the conclusions.

2. FEM formulations

In this work, the FEM based on updated Lagrangian formulation for large-deformation structure [32] is utilized. FEM formulations are given as

$$M_I a_{II} + f_{II}^{\text{int}} = f_{II}^{\text{ext}} \quad (1)$$

$$f_{il}^{\text{int}} = \int_{\Omega} \frac{\partial N_I}{\partial x_j} \sigma_{ji} d\Omega \quad (2)$$

$$f_{il}^{\text{ext}} = \int_{\Omega} N_I \rho b_i d\Omega + \int_{\Gamma_t} N_I \bar{t}_i d\Gamma \quad (3)$$

where M_I is the lumped mass for the node I , a_{il} is the acceleration, f_{il}^{ext} and f_{il}^{int} is equivalent external force and internal force, respectively. And N_I is the shape function of node I , x_j is the coordinate, ρ is the density, σ_{ji} is Cauchy Stress, b_i and \bar{t}_i is body force and surface force, respectively. Furthermore, Γ_t is the boundary of traction, and $d\Omega$ is the area of element.

3. SPH formulations

Here the SPH method is used to solve the conservation equations of mass and linear momentum for fluids, which are given as

$$\frac{1}{\rho} \frac{D\rho}{Dt} + \nabla \bullet \mathbf{v} = 0 \quad (4)$$

$$\frac{D\mathbf{v}}{Dt} = -\frac{1}{\rho} \nabla p + v_0 \nabla^2 \mathbf{v} + \mathbf{f} \quad (5)$$

Discretization of Eqs. (4) and (5) can be written as

$$\frac{D\rho_i}{Dt} = \rho_i \sum_j \frac{m_j}{\rho_j} (\mathbf{v}_i - \mathbf{v}_j) \nabla_i W_{ij} \quad (6)$$

$$\frac{D\mathbf{v}_i}{Dt} = - \sum_j m_j \left(\frac{p_i}{\rho_i^2} + \frac{p_j}{\rho_j^2} + \Pi_{ij} \right) \nabla_i W_{ij} + \sum_j \frac{m_j (v_{oi} + v_{oj}) \mathbf{x}_{ij} \bullet \nabla_i W_{ij}}{\rho_j (\mathbf{x}_{ij}^2 + \eta^2)} \mathbf{v}_{ij} + \mathbf{f} \quad (7)$$

where \mathbf{v} is the velocity vector, \mathbf{f} is the body force, p is the pressure, ρ is the density, m is the mass, \mathbf{x} is position vector, v_o is the viscosity of the fluid. $\mathbf{v}_{ij} = \mathbf{v}_i - \mathbf{v}_j$ and $\mathbf{x}_{ij} = \mathbf{x}_i - \mathbf{x}_j$ is the relative velocity and position of particles, respectively. W is the smoothing kernel function with a smooth length h , and cubic Spline kernel function [33] is used in this paper. $\eta = 0.1h$ is a parameter to avoid zero denominator. Π is the Monaghan artificial viscosity [18], and

$$\Pi_{ij} = \begin{cases} \frac{-\alpha_\pi \bar{c}_{ij}}{\bar{\rho}_{ij}} \frac{h \mathbf{v}_{ij} \bullet \mathbf{x}_{ij}}{\mathbf{x}_{ij}^2}, & \mathbf{v}_{ij} \bullet \mathbf{x}_{ij} < 0 \\ 0, & \mathbf{v}_{ij} \bullet \mathbf{x}_{ij} \geq 0 \end{cases} \quad (8)$$

where α_π is the free parameter depending on problems, $\bar{c}_{ij} = (c_i + c_j)/2$ is the average speed of sound, $\bar{\rho}_{ij} = (\rho_i + \rho_j)/2$ is the average density. The expression of viscous term is proposed by Morris [34], that is

$$(v_o \nabla^2 \mathbf{v})_i = \sum_j \frac{m_j (v_{oi} + v_{oj}) \mathbf{x}_{ij} \bullet \nabla_i W_{ij}}{\rho_j (\mathbf{x}_{ij}^2 + \eta^2)} \mathbf{v}_{ij} \quad (9)$$

The weakly compressible SPH (WCSPH) method is used in this paper, in which the pressure is calculated by an equation of state (EOS) [35] and can be written as

$$p - p_0 = c^2 (\rho - \rho_0) \quad (10)$$

The sound speed of particle must be chosen carefully to ensure that the fluid is very closely incompressible. The calculation of sound speed proposed in Reference [34] is used in this paper, and defined as

$$c^2 \approx \varphi \max \left\{ \frac{v_{\max}^2}{\delta}, \frac{\mu}{\rho_0} \left\{ \frac{v_{\max}^2}{L_0 \delta} \right\}, \frac{F^B L_0}{\delta} \right\} \quad (11)$$

where φ is a problem dependent coefficient, v_{\max} is the maximum value of the fluid velocity, L_0 is a characteristic length, F^B is the magnitude of the body force, and δ is the relative incompressibility or the density variation factor.

The homogeneity of particle distribution is quite significant to the accuracy of SPH models. The highly irregular particle distribution can break down the calculation. In order to prevent irregular particle distributions, an artificial particle displacement is developed by Xu et al. [36]. This is effective if all the particles have the same size, but it has to be modified if particles with variable mass are used. As the ghost particles are produced by dividing the interceptive area in this paper, which will be given in the Section 5, the ghost particles have different size and mass. Then, the artificial displacement is modified as

$$\delta \mathbf{x}_i = \beta \sum_j \frac{\mathbf{x}_{ij}}{|\mathbf{x}_{ij}|^3} r_o^2 \frac{m_j}{m_i} v_{\max} \Delta t \quad (12)$$

and

$$r_o = \sum_{j=1}^{N_f} |\mathbf{x}_{ij}| / N_f \quad (13)$$

where $\delta\mathbf{x}_i$ is an artificial particle displacement, β is a problem dependent parameter, r_o is the cutoff distance, N_f is the number of interior fluid particles in the support domain of particle i .

In order to prevent pressure oscillation due to numerical noises, a density correction algorithm proposed by Yildiz et al. [37] is also used, which can be written as

$$\hat{\rho}_i = \rho_i - \omega \sum_j (\rho_i - \rho_j) W_{ij} / \sum_j W_{ij} \quad (14)$$

where $\hat{\rho}_i$ is the corrected density, and ω is a constant which is set to unit in this paper.

4. Particle inconsistency near the boundary in SPH [22]

For the uniform distributed particles away from boundaries of problem domain in SPH, both the zeroth-order and first-order moments of Eqs. (15) and (16) are approximately satisfied. Therefore, the constant and linear functions can be approximately reproduced, and the SPH method possesses approximately C^1 consistency [38,39]. In discrete form, the zeroth-order and first-order moments of the kernel function can be written as

$$\begin{cases} M_0 = \sum_j W(\mathbf{x} - \mathbf{x}_j, h) \frac{m_j}{\rho_j} \approx 1 \\ \mathbf{M}_1 = \sum_j (\mathbf{x} - \mathbf{x}_j) W(\mathbf{x} - \mathbf{x}_j, h) \frac{m_j}{\rho_j} \approx 0 \end{cases} \quad (15)$$

and similarly, the moments for the derivative of the kernel function can be written as

$$\begin{cases} \mathbf{M}'_0 = \sum_j \nabla_{\mathbf{x}} W(\mathbf{x} - \mathbf{x}_j, h) \frac{m_j}{\rho_j} \approx 0 \\ \mathbf{M}'_1 = \sum_j (\mathbf{x} - \mathbf{x}_j) \nabla_{\mathbf{x}} W(\mathbf{x} - \mathbf{x}_j, h) \frac{m_j}{\rho_j} \approx 1 \end{cases} \quad (16)$$

Considering the SPH approximation in discrete form, the kernel support domain is truncated near the boundaries, then the Eqs. (15) and (16) are not satisfied, which result in errors in the reproduction of constant and linear functions. To restore approximately consistency near the boundary, Eq. (15) is rewritten as a summation over interior fluid particles and ghost particles that represent the boundary

$$\begin{cases} M_0 = \sum_{j \in F}^{N_f} W(\mathbf{x} - \mathbf{x}_j, h) \frac{m_j}{\rho_j} + \sum_{j \in B}^{N_b} W(\mathbf{x} - \mathbf{x}_j, h) \frac{m_j}{\rho_j} \approx 1 \\ \mathbf{M}_1 = \sum_{j \in F}^{N_f} (\mathbf{x} - \mathbf{x}_j) W(\mathbf{x} - \mathbf{x}_j, h) \frac{m_j}{\rho_j} + \sum_{j \in B}^{N_b} (\mathbf{x} - \mathbf{x}_j) W(\mathbf{x} - \mathbf{x}_j, h) \frac{m_j}{\rho_j} \approx 0 \end{cases} \quad (17)$$

and Eq. (16) becomes

$$\begin{cases} \mathbf{M}'_0 = \sum_{j \in F}^{N_f} \nabla_{\mathbf{x}} W(\mathbf{x} - \mathbf{x}_j, h) \frac{m_j}{\rho_j} + \sum_{j \in B}^{N_b} \nabla_{\mathbf{x}} W(\mathbf{x} - \mathbf{x}_j, h) \frac{m_j}{\rho_j} \approx 0 \\ \mathbf{M}'_1 = \sum_{j \in F}^{N_f} (\mathbf{x} - \mathbf{x}_j) \nabla_{\mathbf{x}} W(\mathbf{x} - \mathbf{x}_j, h) \frac{m_j}{\rho_j} + \sum_{j \in B}^{N_b} (\mathbf{x} - \mathbf{x}_j) \nabla_{\mathbf{x}} W(\mathbf{x} - \mathbf{x}_j, h) \frac{m_j}{\rho_j} \approx 1 \end{cases} \quad (18)$$

where F represents the set of N_f interior fluid particles and B represents the set of N_b ghost particles of the boundary.

In this paper, the truncated support domain of the kernel function can be recovered to approximately satisfy C^1 consistency by a new ghost particle method, in which the complex geometry boundary is discretized by elements, and the ghost particles are produced by dividing the area of the truncated support domain of kernel function.

5. New ghost particle method

5.1. Dividing interceptive area into subareas corresponding to boundary segments

In order to couple FEM with SPH by using ghost particles, the interceptive area is divided into subareas corresponding to boundary segments, and the subareas can be adopted to produce ghost particles in the Section 5.2. As shown in the Fig. 1, the interceptive area is divided into subareas of Ω_1 , Ω_2 , Ω_3 and Ω_4 , in which Ω_1 , Ω_2 , Ω_3 and Ω_4 correspond to the segment of AB, BC, CD and DF, separately.

The boundary segments which are used to produce subareas for the fluid particle i should be determined firstly. As shown in the Fig. 2, a boundary segment that corresponds to a subarea for fluid particle i should satisfy two conditions. One condition is that the boundary segment cut off the support domain of particle i , the other condition is that the following equation must be satisfied

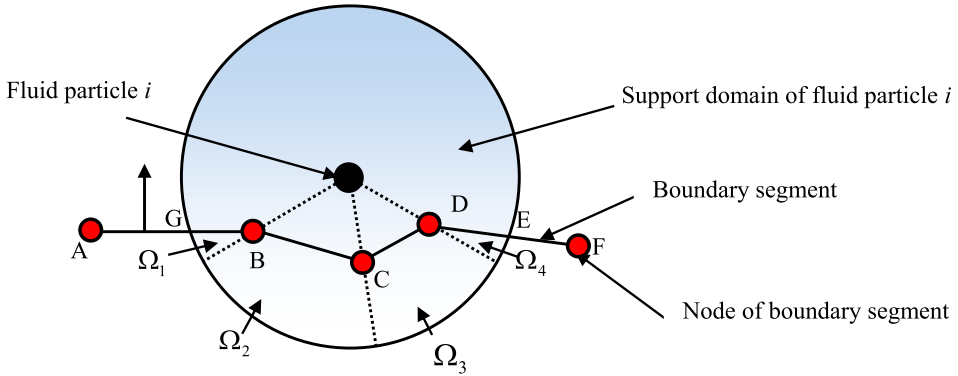


Fig. 1. Dividing interceptive area into subareas based on boundary segments.

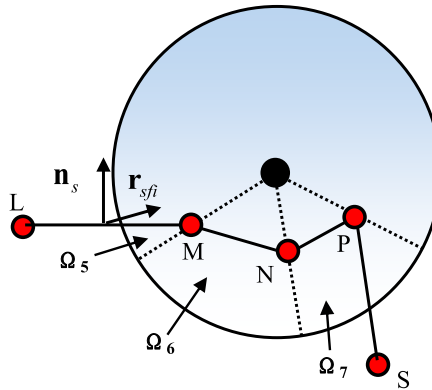


Fig. 2. Determining the boundary segments to produce subareas for fluid particle \$i\$.

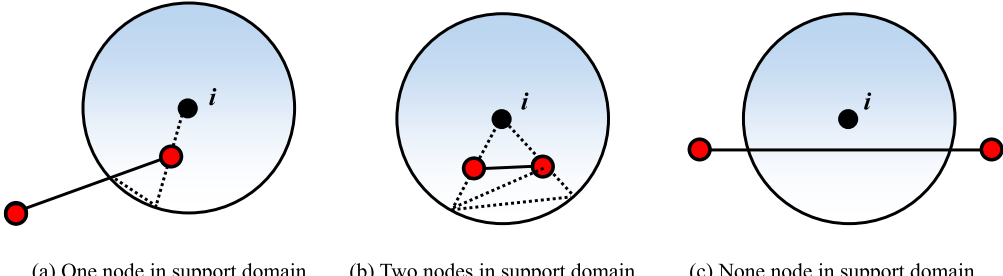


Fig. 3. One segment interacts with one fluid particle.

$$\mathbf{n}_s \bullet \mathbf{r}_{sfi} > 0 \quad (19)$$

where \mathbf{n}_s is the unit outer normal vector of the boundary segment, and \mathbf{r}_{sfi} is the position vector from the central point of boundary segment to the fluid particle \$i\$. For example in the Fig. 2, boundary segments LM, MN and NP correspond to subareas of Ω_5 , Ω_6 and Ω_7 for particle \$i\$, but the boundary segment PS does not correspond to any subarea, because the Eq. (19) is not satisfied.

5.2. Dividing subarea to produce ghost particles

The element size is arbitrary in this paper for coupled FEM–SPH model except that the element size satisfies the requirement of computational accuracy of FEM, then there are three cases between the element segment of structure and the fluid particle \$i\$, as shown in the Fig. 3. If the boundary segment corresponds to a subarea for fluid particle \$i\$, the subarea can be constructed by two fundamental shapes of triangle and arch. Then, the ghost particles can be produced by further dividing the fundamental shapes. As the more number of ghost particles is used, the higher accuracy can be obtained, the area size of ghost particles should be limited to less than a critical area \$A_{cr}\$. In this paper, the critical area is set to \$A_{cr} = 0.1A_i\$, where

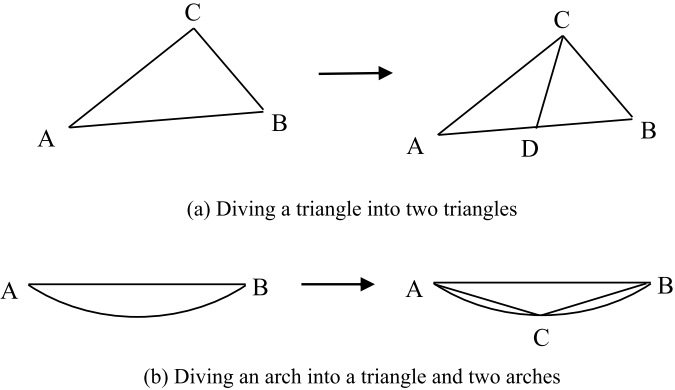


Fig. 4. Dividing the fundamental shapes into small subareas.

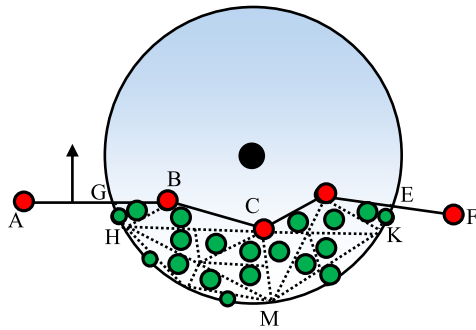


Fig. 5. Ghost particles produced based on small subareas.

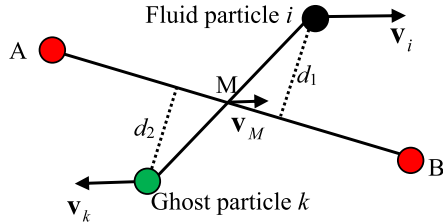


Fig. 6. Velocity of a ghost particle.

A_i is the area of fluid particle i . For a triangle in the Fig. 4(a), if the area of triangle is larger than the critical area A_{cr} , the triangle is divided into two triangles by using the midpoint of the longest edge. For an arch in the Fig. 4(b), it is divided into two arches and a triangle when the area of arch larger than the critical area A_{cr} . Then the ghost particles are produced based on triangles and arches as shown in the Fig. 5. The ghost particles are produced automatically for every fluid particle at each time step, and it can handle the moving boundary and ensure the computational accuracy of SPH method.

Using the small subarea of triangle to produce a ghost particle, the central position of the ghost particle is

$$\mathbf{x}_k = (\mathbf{x}_A + \mathbf{x}_B + \mathbf{x}_C)/3 \quad (20)$$

where \mathbf{x}_A , \mathbf{x}_B and \mathbf{x}_c are coordinates of the triangle's nodes. The central position of the ghost particle produced by an arch is

$$\mathbf{x}_k = \mathbf{x}_{o_arch} \quad (21)$$

where \mathbf{x}_{o_arch} is the centroid coordinate of the arch. The area, density and mass of the ghost particle are

$$VOL_k = S_A \quad (22)$$

$$\rho_k = \rho_i \quad (23)$$

$$m_k = \rho_k \times VOL_k \quad (24)$$

where S_A is the area of triangle or arch, ρ_i is the density of fluid particle i .

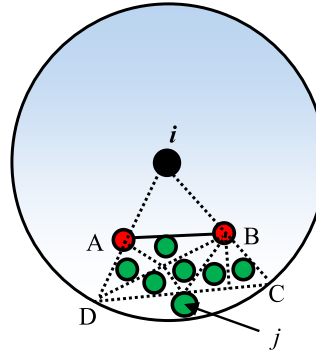


Fig. 7. Ghost particles produced based on subarea ABCD in support domain of fluid particle i .

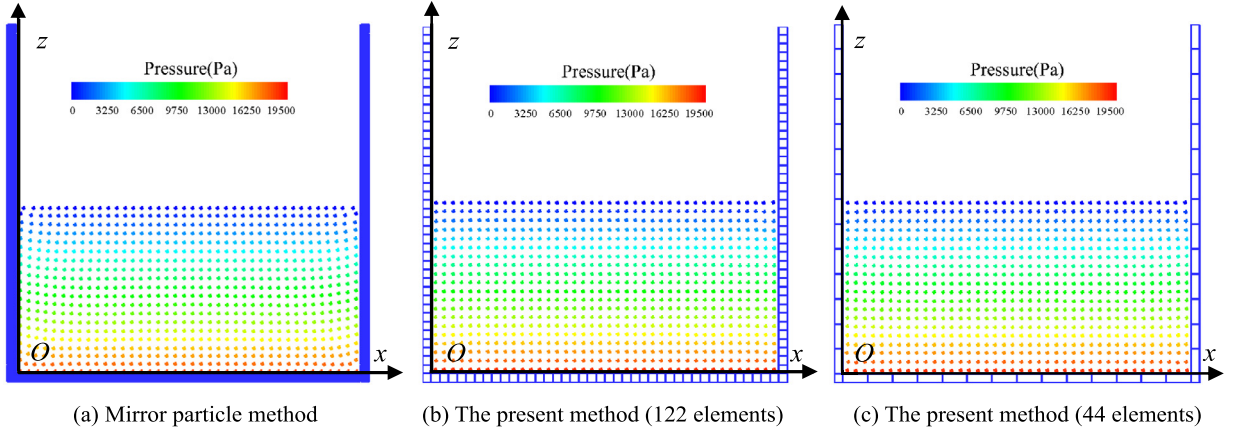


Fig. 8. Particle distribution and pressure field at 5.0 s.

The velocity of a ghost particle is obtained depending on the type of boundary conditions. For the no-slip boundary condition, as shown in the Fig. 6, the velocity of the ghost particle k is assigned according to the method of Takeda et al. [40], that is

$$\mathbf{v}_k = (\mathbf{v}_M - \mathbf{v}_i) \frac{d_2}{d_1} + \mathbf{v}_M \quad (25)$$

where \mathbf{v}_M is the velocity of the point M in segment AB, d_1 and d_2 is the perpendicular distance of the fluid particle i to the segment AB and the ghost particle k to the segment AB, respectively.

6. Coupling SPH with FEM

The FEM is used for solving structure and the SPH is used for simulating fluid in this paper. Using ghost particles for SPH boundary condition, the forces from the elements of structure to the particles of fluid can be exerted through the ghost particles. In order to keep the forces from structure to fluid are equal to the forces from fluid to structure, the opposite forces of the ghost particles to the fluid particles are also exerted on the structure. For example as shown in the Fig. 7, the segment AB interacts with fluid particle i , in which the subarea ABCD is produced based on the segment AB, the force vector from ghost particle j to fluid particle i denote as \mathbf{F}_{GjtF_i} , and the force vector $\mathbf{F}_{S_{ABt}F_i}$ from segment AB to fluid particle i can be written as

$$\mathbf{F}_{S_{ABt}F_i} = \sum_{j \in \Omega_{ABCD}} \mathbf{F}_{GjtF_i} = m_i \left[- \sum_{j \in \Omega_{ABCD}} m_j \left(\frac{p_i}{\rho_i^2} + \frac{p_j}{\rho_j^2} \right) \nabla_i W_{ij} + \sum_{j \in \Omega_{ABCD}} \frac{m_j (\nu_{oi} + \nu_{oj}) \mathbf{x}_{ij} \bullet \nabla_i W_{ij}}{\rho_j (\mathbf{x}_{ij}^2 + \eta^2)} \mathbf{v}_{ij} \right] \quad (26)$$

The vector of opposite forces from the fluid particle i to the segment AB is

$$\mathbf{F}_{F_itS_{AB}} = -\mathbf{F}_{S_{ABt}F_i} \quad (27)$$

and $\mathbf{F}_{F_itS_{AB}}/2$ is applied on node A and node B, respectively.

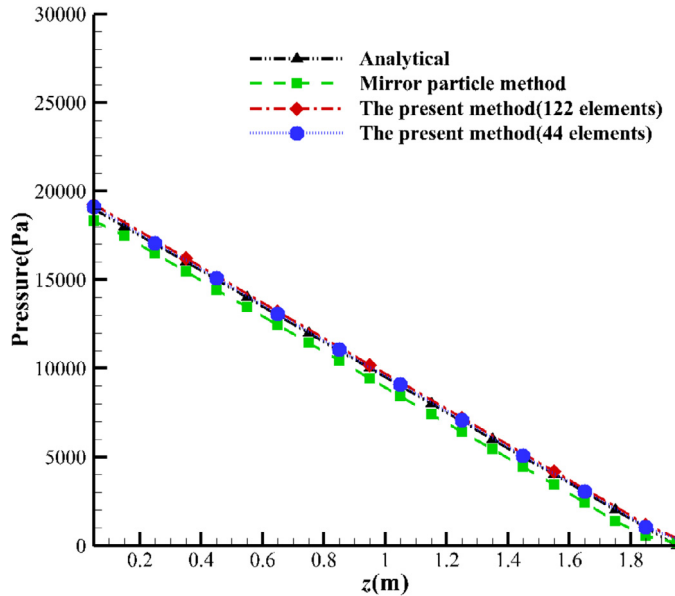


Fig. 9. Hydrostatic pressure at the cross section of $x = 2$ m.

The steps of the new ghost particle technique for coupled FEM–SPH model are as follows:

- (1) Loop over all the segments.
 - (1.1) For a segment, search the fluid particles interacted with the segment.
 - (1.2) Loop over all the fluid particles interacted with the segment.
 - (1.2.1) For a fluid particle and the segment, produce ghost particles for the fluid particle and calculate the corresponding value of fluid particle using ghost particles. Compute the forces from the segment to the fluid particle.
 - (1.2.2) Apply the opposite forces of the fluid particle on the segment.
 - (1.3) End the loop of the fluid particles corresponding to the segment.
- (2) End the loop of segments.

7. Simulation for FSI problems

7.1. Still water case

The case of still water in a tank is used to evaluate the moments of the kernel function and its derivative, and it also apply to investigate the performance of the present method. The length and height of the square tank is 4 m, respectively, and the height of water in the tank is 1.95 m. The particle spacing is $\Delta x = 0.1$ m for different models. The speed of sound is $c_0 = 80$ m/s. Artificial viscosity with free parameter $\alpha_\pi = 0.1$ is used in this case. At the beginning of the simulation, the water is at rest and the pressure is hydrostatic. The density and pressure of the ghost particles are calculated by

$$\rho_k = \rho_i + \rho_0 g z_{ik} / c^2 \quad (28)$$

$$p_k = p_i + \rho_0 g z_{ik} \quad (29)$$

$$z_{ik} = z_i - z_k \quad (30)$$

where z is the coordinate of depth and g is the acceleration of gravity. These flow properties resemble hydrostatic conditions and satisfy the Cauchy boundary condition [22].

In order to study on the convergence of the present method, the velocity error norm L_2 is defined as [41]

$$L_2(\mathbf{v}) = \sqrt{\frac{1}{NT} \sum_{i=1}^{NT} (\|\mathbf{v}_i\|)^2} \quad (31)$$

where NT is the total number of fluid particles, and $\|\mathbf{v}_i\|$ denotes the norm length of velocity vector.

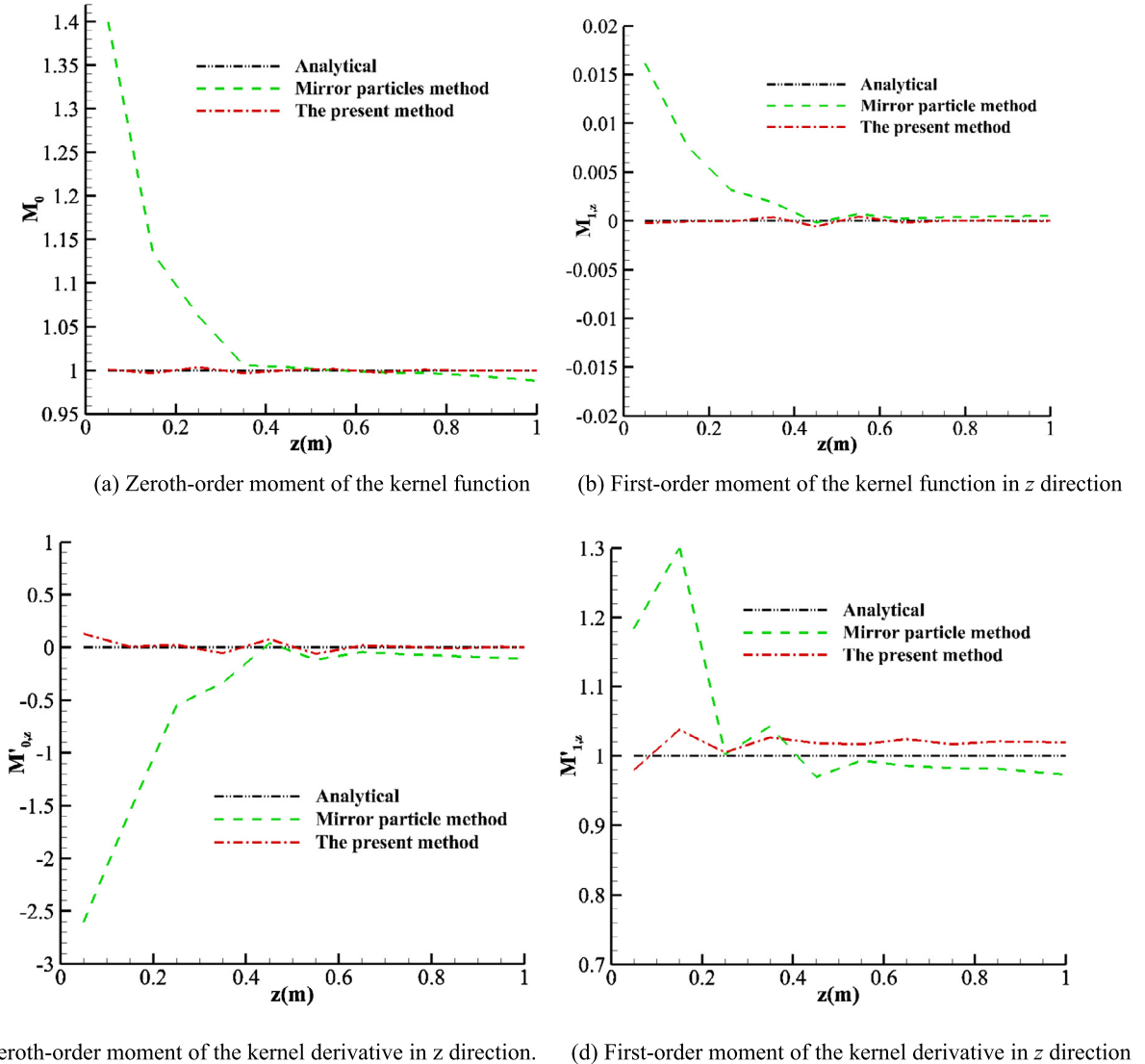


Fig. 10. Moments of the kernel function and its derivative at 5 s.

[Fig. 8](#) shows the particle distribution and the pressure field of different methods at 5.0 s, in which the tank is discretized by 122 and 44 quadrilateral elements, respectively, as shown in the [Figs. 8\(b\)](#) and [\(c\)](#). It can be observed that the pressure field is the same between [Fig. 8\(b\)](#) and [Fig. 8\(c\)](#), and the boundary with different size of elements for rigid tank is insensitive to the present new ghost particle method. [Fig. 8](#) also indicates that the present ghost particle method is more accurate than the mirror particle method, and the corners of the fluid are curved numerically for the particle distribution obtained by the mirror particle method. Furthermore, [Fig. 9](#) shows the hydrostatic pressure obtained by the present method at the cross section of $x = 2$ m compared with analytical solution when $t = 5.0$ s. It can be seen that the pressure calculated by the present ghost particle method is more accurate than the mirror particle method, and the pressure calculated by the present ghost particle method with 122 elements is the same with that of 44 elements.

In the [Fig. 10](#), the zeroth-order and first-order moments of kernel function and its derivative in z direction are plotted along the cross section of $x = 2.0$ m at 5 s, in which the tank is discretized by 122 quadrilateral elements. For the analytical results, the zeroth-order moment has a value of unity, the first-order moment should be zero, and their derivative values are zero and unity, respectively. It can be concluded that the accuracy of the moments of kernel function and its derivative can be significant improved by the present method compared with the mirror particle method. [Fig. 11](#) shows that the zeroth-order moment of kernel function at position (2, 0.05) changes over time, at the beginning of time, the zeroth-order moments of kernel function obtained by the mirror particle method and the present method are both in good agreement with analytical results. However, the error of zeroth-order moment of kernel function obtained by the mirror particle method increase quickly until 4 s. This is because the distribution of mirror particles completely depend on the

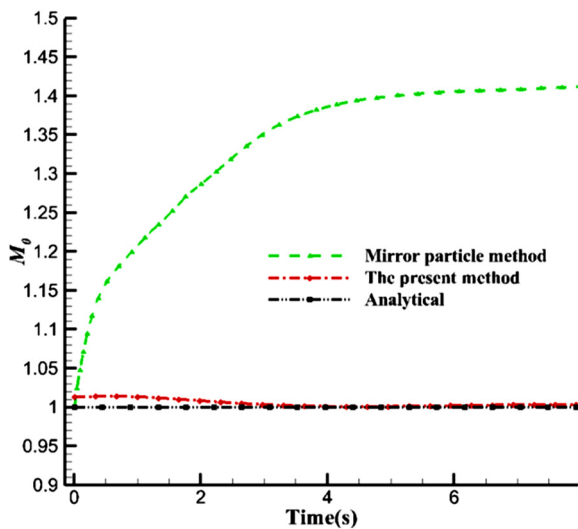


Fig. 11. Zeroth-order moment of the kernel function at position (2, 0.05) changes over time.

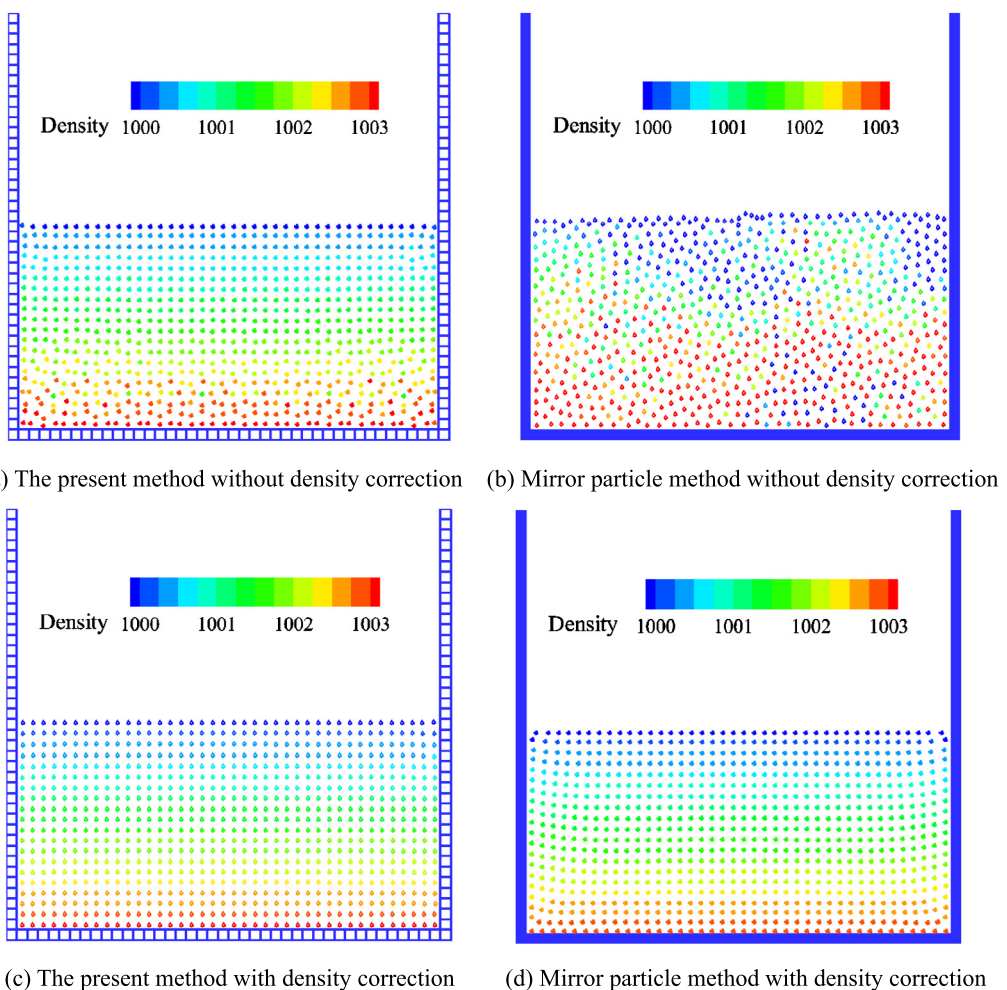


Fig. 12. Density field at 5 s for the still water case.

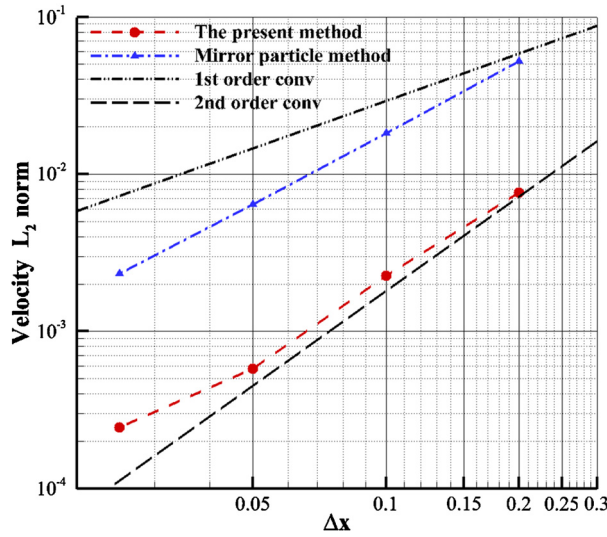


Fig. 13. Convergence of velocity error norm L_2 for still water case.

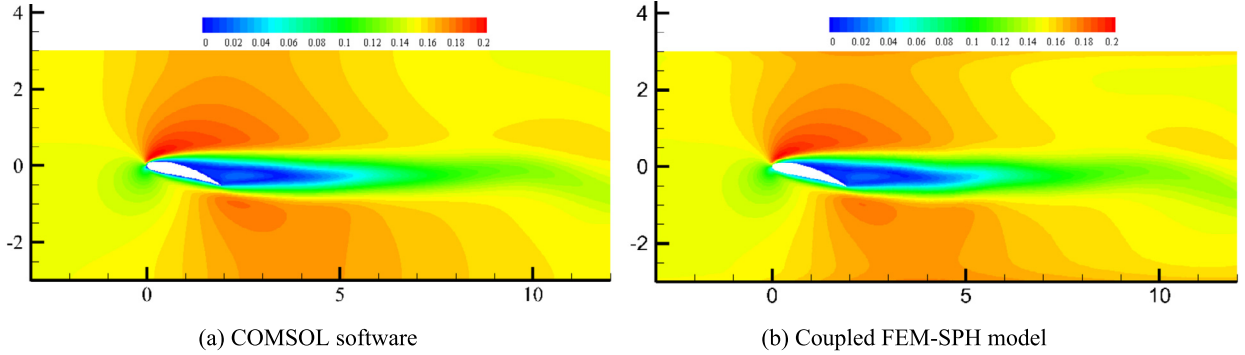


Fig. 14. Velocity contours for the attack angle of 15° at $Re = 300$.

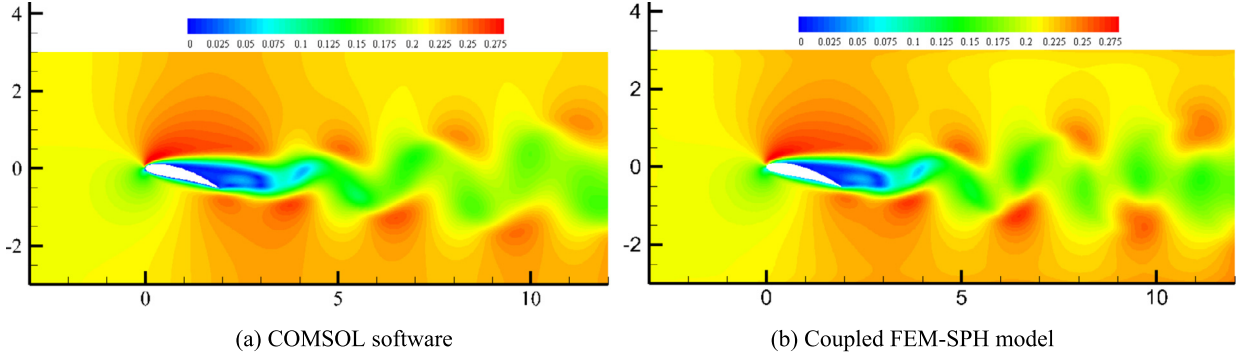
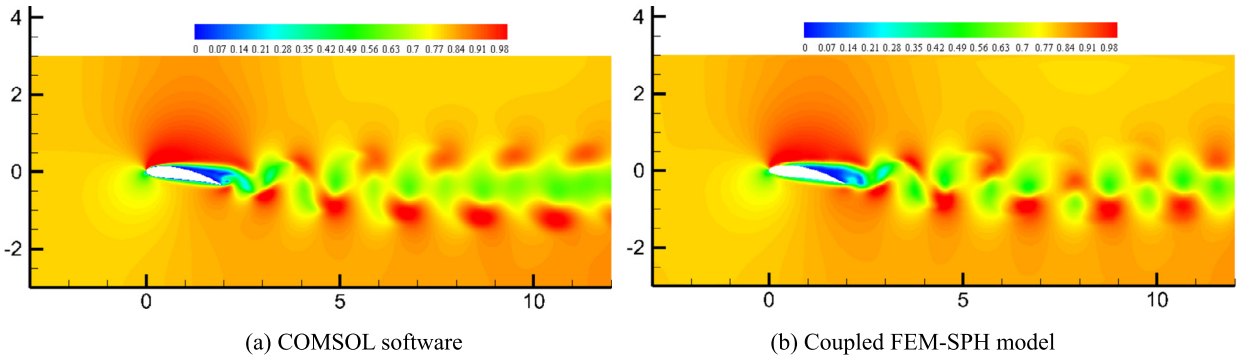
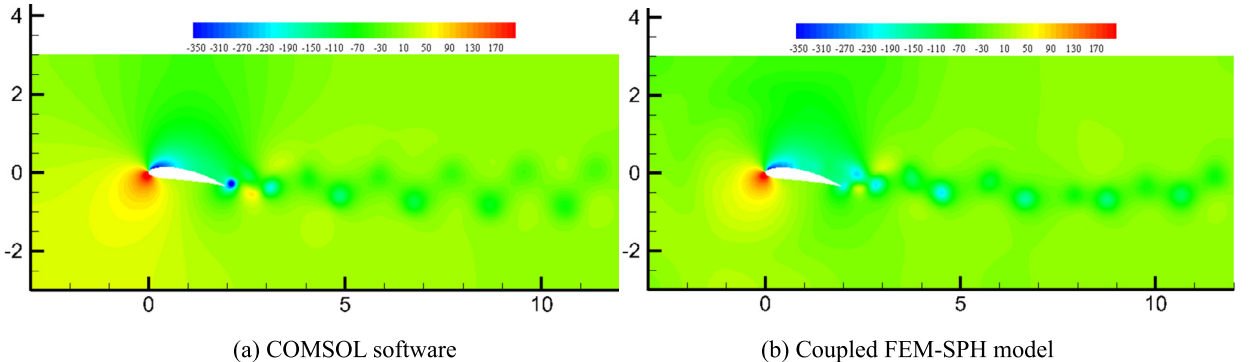
fluid particles, when the fluid particles are close to the bottom wall under the gravity, the mirror particles will be also close to the bottom wall. The unreasonable distribution of fluid particles and mirror particles makes the particle volumes are overlapped each other near the boundary, then the error of zeroth-order moment of kernel function can be increased. The error near the boundary can be suspended because the ghost particles do not depend on the distribution of fluid particles in the present method.

Although there are large errors for the moments of kernel function and its derivative with the mirror particle method, but there is no large density error for the mirror particle method with density correction algorithm [37]. Fig. 12 shows the density field at 5 s, it can be seen that the smooth and reasonable densities are obtained by the mirror particle method and the present method with density correction algorithm, the densities distribute unevenly if the density correction algorithm is not used in the calculating process. Fig. 13 shows the convergence of velocity error norm L_2 , the present ghost particle method can obtain better accuracy and higher convergence than that obtained by the mirror particle method when the same particle resolution is used. The results indicate that the accuracy of the moments of kernel function and its derivative near the boundary are important for the whole numerical model.

7.2. The flow around the airfoil obstacle placed inside the channel

In order to test the ability for treating complex geometry boundary discretized by elements, we have solved a two-dimensional problem of a flow around a NACA airfoil [42]. The conservation equations of mass and linear momentum are solved for the test case on a rectangular domain with the length of $L = 15$ m and the height of $H = 6$ m. The density of fluid is $\rho_f = 1000 \text{ kg/m}^3$. The kinematic viscosity of fluid is $\nu_f = 0.001 \text{ m}^2/\text{s}$. The body force in x -direction is $F_y^B = 0.003 \text{ N/kg}$. Artificial viscosity with free parameter $\alpha_\pi = 0$ is used in this case.

Boundary conditions for inlet and outlet particles are implemented that particles crossing the outflow boundary are reinserted into the flow domain at the inlet. The inlet boundary condition is that the velocity is prescribed, and the outflow condition is that the pressure is prescribed to be 0. For the upper and lower walls, the symmetry boundary condition for

**Fig. 15.** Velocity contours for the attack angle of 15° at Re = 420.**Fig. 16.** Velocity contours for the attack angle of 10° at Re = 1600.**Fig. 17.** Pressure contours for the attack angle of 10° at Re = 1600.

the velocity is applied. The no-slip boundary condition is implemented for the NACA airfoil obstacle. NACA airfoil with a chord length of 2 m is created by

$$y_c = \begin{cases} m_c(2p_c x_c - x_c^2)/p_c^2, & 0 \leq x_c \leq p_c \\ m_c(2p_c(x_c - 1) + 1 - x_c^2)/(1 - p_c)^2, & p_c < x_c \leq 1 \end{cases} \quad (32)$$

where x_c and y_c are the coordinates of mean camber line. m_c is the maximum camber in percentage of the chord which is taken to be 5%. p_c is the position of the maximum camber in percentage of the chord that is set to be 50%. The thickness distribution above and below the mean camber line is calculated as

$$y_t = 5t_t(0.2969x_c^{0.5} - 0.126x_c - 0.3516x_c^2 + 0.284x_c^3 - 0.1015x_c^4) \quad (33)$$

in which t_t is the maximum thickness of the airfoil in percentage of chord which is 15%. The final coordinates of the airfoil for the upper surface (x_U, y_U) and the lower surface (x_L, y_L) are determined by

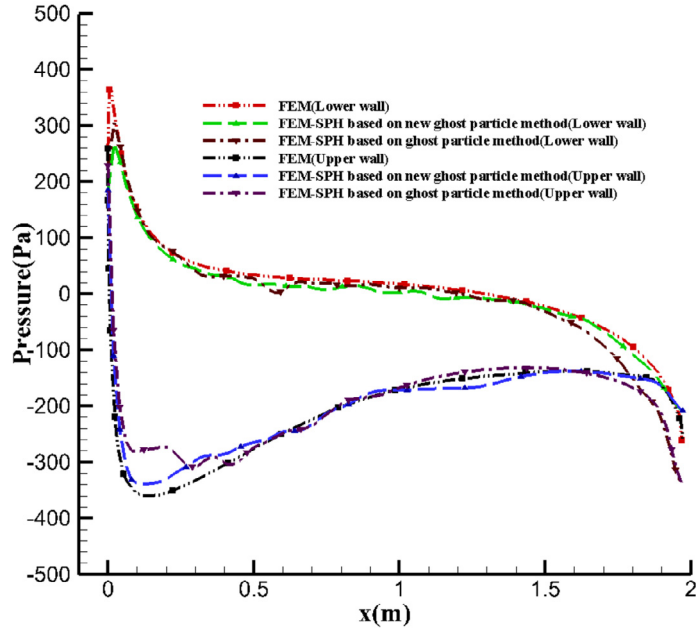


Fig. 18. Comparison of pressure envelopes for the attack angle of 10° at $Re = 1600$.

Table 1
Results of the FSI benchmark test.

	y -displacement (10^{-3})		f_0
	max	min	
Turek [44]	82.94	-80.46	1.93
FEM-SPH	92.35	-88.20	1.915

$$\begin{aligned} x_U &= x_c - y_t \sin \phi \\ y_U &= y_c + y_t \cos \phi \\ x_L &= x_c + y_t \sin \phi \\ y_L &= y_c - y_t \cos \phi \\ \phi &= \arctan(dy_c/dx_c) \end{aligned} \quad (34)$$

In the present method, 102022 particles are used for fluid and 3274 quadrilateral elements are used for solid. The convergence analysis is conducted for FEM model with 45574, 93640, 122176 and 153380 triangular elements using COMSOL software, the results of FEM model using 122176 elements are quite close to those of FEM model using 153380 elements, then the results of FEM model with 153380 elements can be used as the reference values to compare with the FEM-SPH models. Fig. 14 and Fig. 15 compare the velocity contours obtained by COMSOL software and the present coupled FEM-SPH model for the attack angles of 15° at the Reynolds numbers of 300 and 420, respectively. Fig. 16 and Fig. 17 show the comparison of the velocity contours and pressure contours for the attack angles of 10° at $Re = 1600$, respectively. It can be seen from the Figs. 14–17 that the results obtained by the coupled FEM-SPH model show the same trend compared with those of COMSOL software results. Fig. 18 shows the comparison of pressure envelopes for the attack angle of 10° at $Re = 1600$, in which the resolutions of the FEM-SPH model based on the previous ghost particle method [21] are the same as those of the present method. It indicates that the results of the present method are in good agreement with the COMSOL software results, and the results of FEM-SPH model based on the new ghost particle method are better than the results of FEM-SPH model based on the previous ghost particle method [21] compared with the results obtained by COMSOL software, especially for the tail of airfoil obstacle. This case shows the ability that the coupled FEM-SPH model based on the new ghost particle method can handle complex geometry boundary which discretized by elements.

7.3. The FSI benchmark case

The FSI benchmark case defined by Turek and Hron [43] is simulated in this paper, as shown in the Fig. 19, in which the flow past a fixed circular cylinder with a flexible bar is analyzed. The computational domain has length $L = 2.50$ m and height $H = 0.41$ m. The circle center is located at $C = (0.2, 0.2)$, which measured from the left bottom corner of the channel,

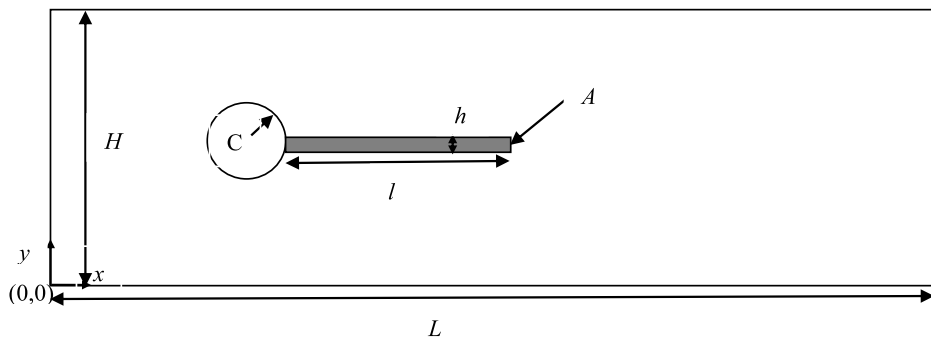


Fig. 19. Computational domain of the FSI benchmark case.

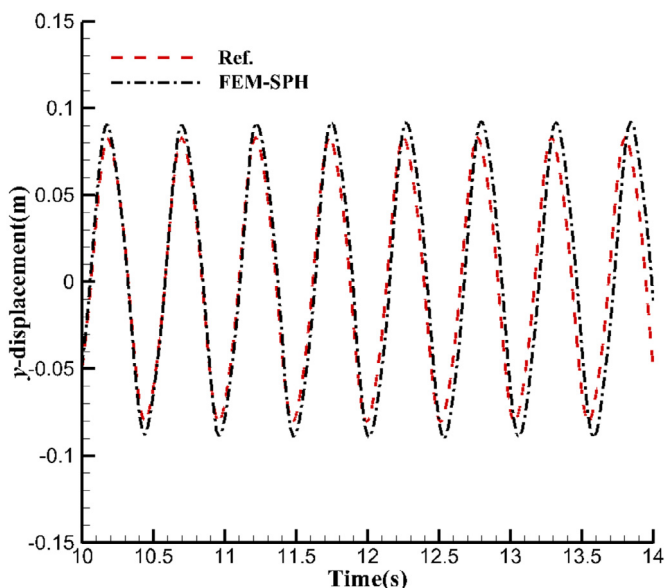


Fig. 20. y -displacement of control point A compared with results of Turek [44].

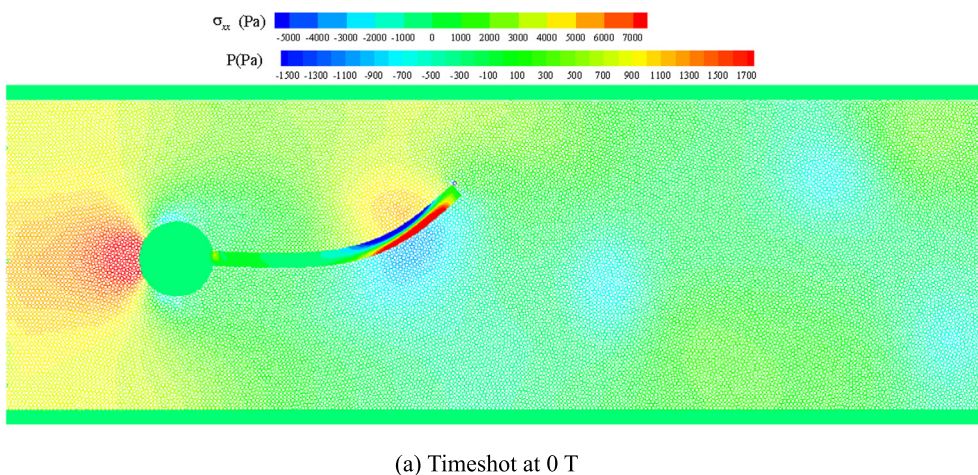
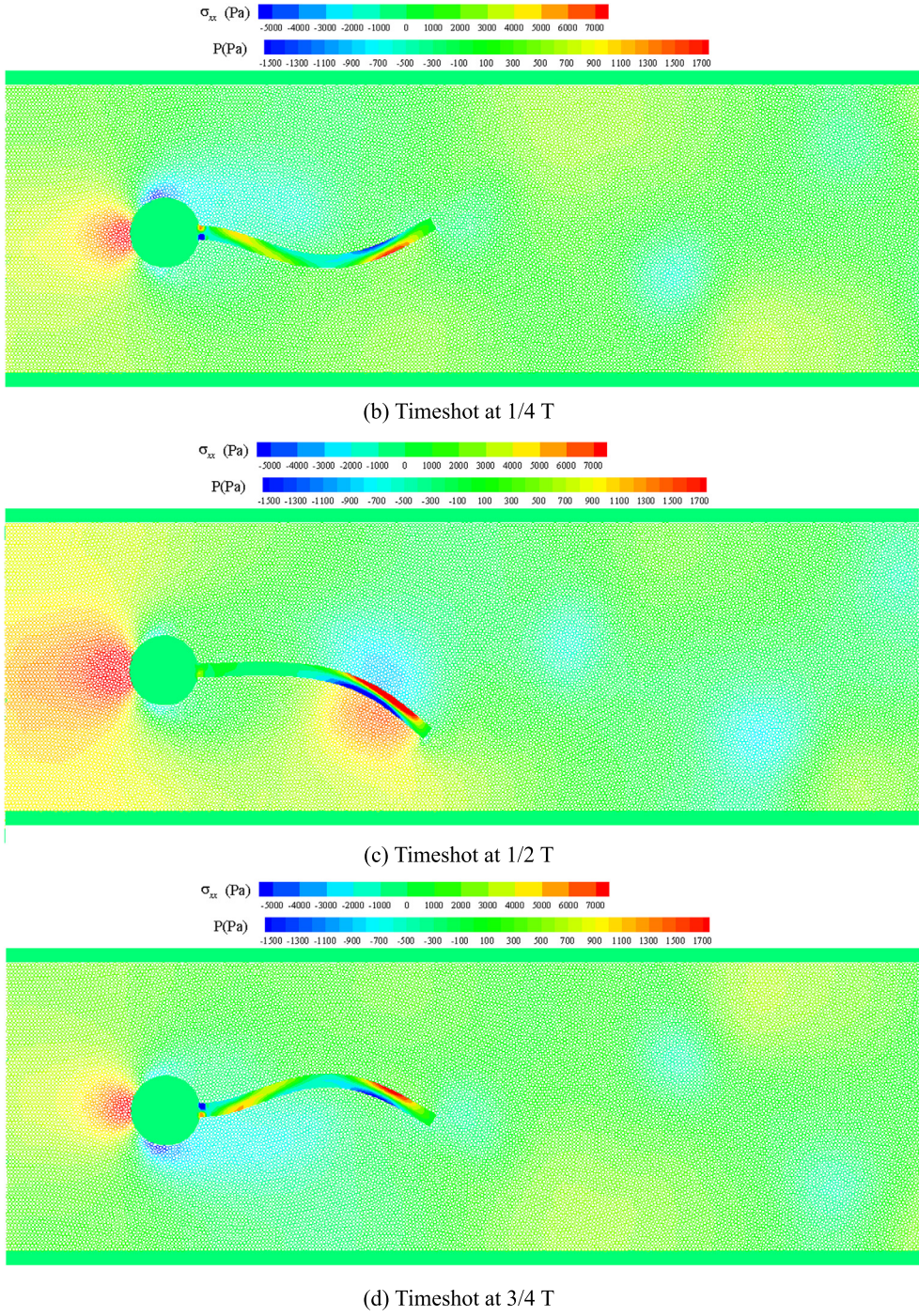


Fig. 21. Fluid particles colored by contour of pressure and FEM nodes colored by contour of lateral stress σ_{xx} .

**Fig. 21.** (continued)

and the radius of the circle is $r = 0.05$. The elastic structure bar has length $l = 0.35$ m and height $h = 0.02$ m, the right bottom corner of the bar is located at $(0.6, 0.19)$ and the left end is fully attached to the fixed cylinder. The control point $A(t)$ is attached to the structure and moved in initial time with $A(0) = (0.6, 0.2)$. The density of fluid is $\rho_f = 1000 \text{ kg/m}^3$. The kinematic viscosity of fluid is $\nu_f = 0.001 \text{ m}^2/\text{s}$. The material properties of flexible bar are density $\rho_s = 10000 \text{ kg/m}^3$, Young modulus $E = 1.4 \times 10^6 \text{ N/m}^2$ and Poisson ratio $\nu_s = 0.4$. The speed of sound is $c = 25 \text{ m/s}$. Artificial viscosity with free parameter $\alpha_\pi = 0$ is used in this case. The particle spacing is $\Delta x = 0.005 \text{ m}$ corresponding to 41224 particles. And the number of quadrilateral element is 360 and 643 for flexible bar and rigid part, respectively, in which the rigid part contains the fixed circular cylinder and the top/button walls.

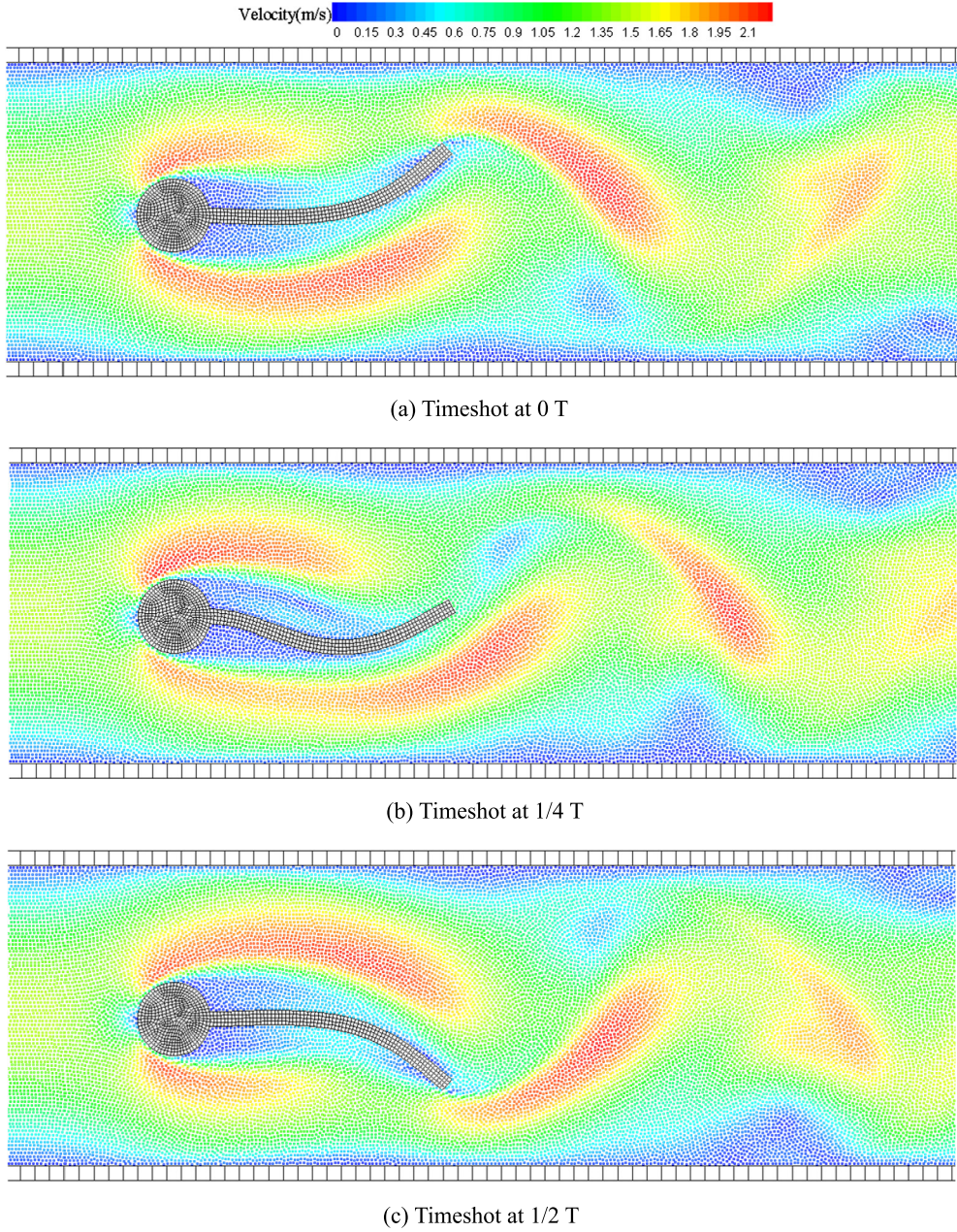


Fig. 22. Velocity distribution for four timeshots in an oscillation cycle.

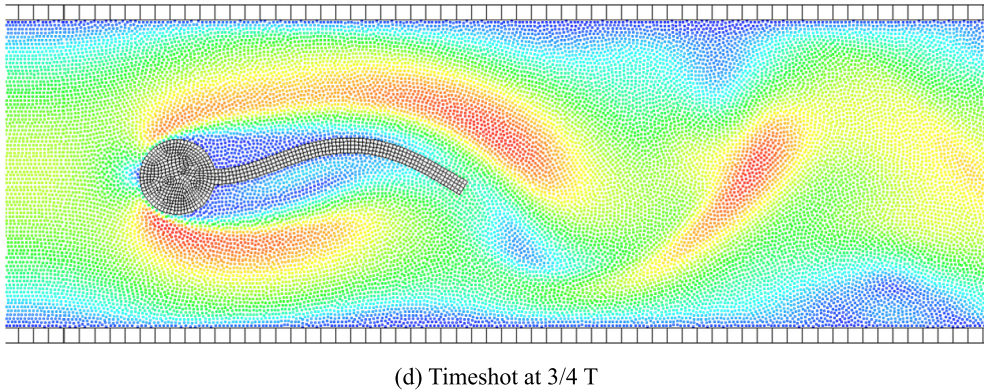
The inflow condition is from the left only and a parabolic velocity profile is given as

$$v_x^{\text{in}}(0, y) = 1.5\bar{U} \frac{4.0}{0.1681} y(0.41 - y) \quad (35)$$

where \bar{U} is the mean inflow velocity and $\bar{U} = 1$ m/s is used in this paper. The inflow velocity suggested by Turek and Hron [43] is used as the following

$$v_x^{\text{in}}(t, 0, y) = \begin{cases} v_x^{\text{in}}(0, y) \frac{1-\cos(\pi t/2)}{2}, & \text{if } t < 2.0 \\ v_x^{\text{in}}(0, y), & \text{otherwise} \end{cases} \quad (36)$$

The outflow condition is that the pressure is prescribed to be 0. The no-slip condition is applied for all the interface between fluid and structure.



(d) Timeshot at 3/4 T

Fig. 22. (continued)

Table 1 shows the quantitative comparison of the present results and reference results [44]. The fundamental frequency f_0 is that of the y -displacement of the trailing edge. Fig. 20 presents y -displacement compared with reference results of Turek [44]. The results obtained by the present coupled FEM-SPH model are in good agreement with the Turek's results [44]. In the Fig. 21, the fluid particles colored by contour of pressure and the FEM nodes colored by contour of lateral stress σ_{xx} are presented for four timeshots in an oscillation cycle, where T denotes an oscillation cycle. Fig. 22 shows the velocity distribution for four timeshots in an oscillation cycle. It can be seen that the results of fluid–structure interaction are in good agreement with the results found in the literature [44]. It indicates that the present coupled FEM-SPH model has good performance for simulating FSI problems, and the moving interface can be easily handled with good accuracy. On the other hand, it can also be seen from the Fig. 21 that concentration of stress at the corners of flexible bar can also be obtained in the present coupled FEM-SPH model.

8. Conclusions

In this paper, a new ghost particle method is proposed to couple FEM with SPH for solving FSI problems. The new ghost particle method can obtain approximate C^1 consistency near the boundary and can handle the complex geometry boundary and moving boundary discretized by elements. In the present ghost particle method, the ghost particles are produced automatically at each time step for every fluid particle. The opposite force vector from the structure segment to the fluid particle is equal to the force vector from the fluid particle to the structure segment. So the equation of momentum is conservation in the coupled FEM-SPH model for FSI problems. Moreover, the size of elements does not need to match the size of the particles for the present coupled FEM-SPH model based on the new ghost particle method.

Numerical cases of this paper indicate that the new ghost particle method is more accurate and higher convergence than the mirror particle method for the FSI problems, and the present method is robust for simulating complex geometry boundary and moving boundary discretized by elements.

Acknowledgements

The supports from National Natural Science Foundation of China (11272118, 11372106) and Natural Science Foundation of Hunan Province (2016JJ1009) are gratefully acknowledged.

References

- [1] R. Bennet, J. Edwards, An overview of recent developments in computational aeroelasticity, in: The 29th AIAA Fluid Dynamics Conference, Albuquerque, NM, 1998.
- [2] R. van Loon, F.N. van de Vosse (Eds.) in: Fluid–Structure Interaction in Biomedical Applications, Int. J. Numer. Methods Biomed. Eng. 26 (2010) 273–275.
- [3] C.A. Taylor, C.A. Figuerola, Patient-specific modeling of cardiovascular mechanics, Annu. Rev. Biomed. Eng. 11 (2009) 109–134.
- [4] O.F. Otooby, A.G. Malan, A matrix-free, implicit, incompressible fractional-step algorithm for fluid–structure interaction applications, J. Comput. Phys. 231 (2012) 5389–5405.
- [5] P. Brandimarte, Finite-Difference Methods for Partial Differential Equations, Wiley, 1960.
- [6] H.K. Versteeg, W. Malalasekera, An Introduction to Computational Fluid Dynamics: The Finite Volume Method, Longman, 1995.
- [7] C.W. Hirt, A.A. Amsden, J.L. Cook, An arbitrary Lagrangian–Eulerian computing method for all flow speeds, J. Comput. Phys. 14 (1974) 227–253.
- [8] J. Donea, S. Giuliani, J.P. Halleux, An arbitrary Lagrangian–Eulerian finite element method for transient dynamic fluid–structure interactions, Comput. Methods Appl. Mech. Eng. 33 (1982) 689–723.
- [9] K. Morinishi, T. Fukui, An Eulerian approach for fluid–structure interaction problems, Comput. Fluids 65 (2012) 92–98.
- [10] T.D. Vuyst, R. Vignjevic, J.C. Campbell, Coupling between meshless and finite element methods, Int. J. Impact Eng. 31 (2005) 1054–1064.
- [11] P.H.L. Groenboom, B.K. Cartwright, Hydrodynamics and fluid–structure interaction by coupled SPH-FE method, J. Hydraul. Res. 48 (2009) 61–73.
- [12] G. Fourey, G. Oger, D. Touzé, B. Alessandrini, Violent fluid–structure interaction simulations using a coupled SPH/FEM method, in: Proc. IOP Conference Series: Materials Science and Engineering, IOP Publishing, 2010, p. 012041.

- [13] Q. Yang, V. Jones, L. Mccue, Free-surface flow interactions with deformable structures using an SPH–FEM model, *Ocean Eng.* 55 (2012) 136–147.
- [14] L.B. Lucy, A numerical approach to the testing of the fission hypothesis, *Astron. J.* 82 (1977) 1013–1024.
- [15] R.A. Gingold, J.J. Monaghan, Smoothed particle hydrodynamics – theory and application to non-spherical stars, *Mon. Not. R. Astron. Soc.* 181 (1977) 375–389.
- [16] J.J. Monaghan, R.A. Gingold, Shock simulation by the particle method SPH, *J. Comput. Phys.* 52 (1983) 374–389.
- [17] J.J. Monaghan, J.B. Kajtar, SPH particle boundary forces for arbitrary boundaries, *Comput. Phys. Commun.* 180 (2009) 1811–1820.
- [18] J.J. Monaghan, Simulating free surface flows with SPH, *J. Comput. Phys.* 110 (1994) 399–406.
- [19] S.J. Cummins, T.B. Silvester, P.W. Cleary, Three-dimensional wave impact on a rigid structure using smoothed particle hydrodynamics, *Int. J. Numer. Methods Fluids* 68 (2012) 1471–1496.
- [20] X.Y. Hu, N.A. Adams, A multi-phase SPH method for macroscopic and mesoscopic, *J. Comput. Phys.* 213 (2006) 844–861.
- [21] M. Yildiz, R.A. Rook, A. Suleman, SPH with multiple boundary tangent method, *Int. J. Numer. Methods Eng.* 77 (2009) 1416–1438.
- [22] G. Fournakas, R. Vacondio, B.D. Rogers, On the approximate zeroth and first-order consistency in the presence of 2-D irregular boundaries in SPH obtained by the virtual boundary particle methods: approximate zeroth and first-order consistent solid boundaries in SPH, *Int. J. Numer. Methods Fluids* 78 (2015) 475–501.
- [23] D.J. Barker, P. Brito-Parada, S.J. Neethling, Application of B-splines and curved geometries to boundaries in SPH, *Int. J. Numer. Methods Fluids* 76 (2014) 51–68.
- [24] S. Kulasegaram, J. Bonet, R.W. Lewis, M. Profit, A variational formulation based contact algorithm for rigid boundaries in two-dimensional SPH applications, *Comput. Mech.* 33 (2004) 316–325.
- [25] M. Ferr, D.R. Laurence, B.D. Rogers, D. Violeau, C. Kassiotis, Unified semi-analytical wall boundary conditions for inviscid, laminar or turbulent flows in the meshless SPH method, *Int. J. Numer. Methods Fluids* 71 (2013) 446–472.
- [26] J. Feldman, J. Bonet, Dynamic refinement and boundary contact forces in SPH with applications in fluid flow problems, *Int. J. Numer. Methods Eng.* 72 (2007) 295–324.
- [27] A. Mayrhofer, B.D. Rogers, D. Violeau, M. Ferrand, Investigation of wall bounded flows using SPH and the unified semi-analytical wall boundary conditions, *Comput. Phys. Commun.* 184 (2013) 2515–2527.
- [28] S.W. Attaway, M.W. Heinstein, J.W. Swegle, Coupling of smooth particle hydrodynamics with the finite element method, *Nucl. Eng. Des.* 150 (1994) 199–205.
- [29] Z. Zhang, H. Qiang, W. Gao, Coupling of smoothed particle hydrodynamics and finite element method for impact dynamics simulation, *Eng. Struct.* 33 (2011) 255–264.
- [30] S. Swaddiwudhipong, M.J. Islam, Z.S. Liu, High velocity penetration/perforation using coupled smooth particle hydrodynamics-finite element method, *Int. J. Protect. Struct.* 1 (2012).
- [31] A. Danilewicz, Z. Sikora, Numerical simulation of crater creating process in dynamic replacement method by smooth particle hydrodynamics, *Stud. Geotech. Mech.* 36 (2015) 3–8.
- [32] G.R. Johnson, R.A. Stryk, T.J. Holmquist, S.R. Beissel, G.R. Johnson, R.A. Stryk, T.J. Holmquist, S.R. Beissel, Numerical Algorithms in a Lagrangian Hydrocode, 1997.
- [33] J.J. Monaghan, J.C. Lattanzio, J.J. Monaghan, J.C. Lattanzio, A refined particle method for astrophysical problems, *Astron. Astrophys.* 149 (1985) 135–143.
- [34] J.P. Morris, P.J. Fox, Y. Zhu, Modeling low Reynolds number incompressible flows using SPH, *J. Comput. Phys.* 136 (1997) 214–226.
- [35] C. Antoci, M. Gallati, S. Sibilla, Numerical simulation of fluid–structure interaction by SPH, *Comput. Struct.* 85 (2007) 879–890.
- [36] R. Xu, P. Stansby, D. Laurence, Accuracy and stability in incompressible SPH (ISPH) based on the projection method and a new approach, *J. Comput. Phys.* 228 (2009) 6703–6725.
- [37] M. Ozbulut, M. Yildiz, O. Goren, A numerical investigation into the correction algorithms for SPH method in modeling violent free surface flows, *Int. J. Mech. Sci.* 79 (2013) 56–65.
- [38] T. Belytschko, Y. Krongauz, J. Dolbow, C. Gerlach, On the completeness of meshfree particle methods, *Int. J. Numer. Methods Eng.* 43 (1998) 785–819.
- [39] M.B. Liu, G.R. Liu, Restoring particle consistency in smoothed particle hydrodynamics, *Appl. Numer. Math.* 56 (2006) 19–36.
- [40] H. Takeda, S.M. Miyama, M. Sekiya, Numerical simulation of viscous flow by smoothed particle hydrodynamics, *Prog. Theor. Phys.* 92 (1994) 939–960.
- [41] R. Vacondio, B.D. Rogers, P.K. Stansby, Smoothed particle hydrodynamics: approximate zero-consistent 2-D boundary conditions and still shallow-water tests, *Int. J. Numer. Methods Fluids* 69 (2012) 226–253.
- [42] M.S. Shadloo, A. Zainali, M. Yildiz, A. Suleman, A robust weakly compressible SPH method and its comparison with an incompressible SPH, *Int. J. Numer. Methods Eng.* 89 (2012) 939–956.
- [43] S. Turek, J. Hron, Proposal for Numerical Benchmarking of Fluid–Structure Interaction Between an Elastic Object and Laminar Incompressible Flow, 2007.
- [44] Turek, FEATFLOW web page in, http://www.featflow.de/en/benchmarks/cfdbenchmarking/fsi_benchmark.html, 2014.